Revealing electronic correlations in YNi2B2C using photoemission spectroscopy

Aki Pulkkinen, Geoffroy Kremer, Vladimir Strocov, Frank Weber, Ján Minár, Claude Monney

communications physics

A Nature Portfolio journal

Article

https://doi.org/10.1038/s42005-025-02180-4

Revealing electronic correlations in YNi_2B_2C using photoemission spectroscopy

Aki Pulkkinen [1,2], Geoffroy Kremer [2,3], Vladimir N. Strocov [4], Frank Weber [5], Ján Minár [1] ✉ & Claude Monney [2] ✉

The low-energy electronic structure of materials is crucial to understanding and modeling their physical properties. Angle-resolved photoemission spectroscopy (ARPES) is the best experimental technique to measure this electronic structure, but its interpretation can be delicate. Here we use a combination of density functional theory (DFT) and one-step model of photoemission to decipher the soft x-ray ARPES spectra of the quaternary borocarbide superconductor YNi_2B_2C. Our analysis reveals the presence of moderate electronic correlations beyond the semilocal DFT within the generalized gradient approximation. We show that DFT and the full potential Korringa-Kohn-Rostoker method combined with the dynamical mean field theory (DFT+DMFT) with average Coulomb interaction $U = 3.0$ eV and the exchange energy $J = 0.9$ eV applied to the Ni d-states are necessary for reproducing the experimentally observed SX-ARPES spectra.

YNi_2B_2C is an intermetallic borocarbide superconductor[1] in the family RNi_2B_2C (R = Y, Lu, Tm, Er, Ho), with superconducting transition temperature $T_c = 15.6$ K. Identified early as a conventional phonon-mediated s-wave superconductor[2–6], YNi_2B_2C was later found to show signs of large anisotropy of the superconducting gap[7–18] and strong electron-phonon interactions near the superconducting transition[19] stimulating a theoretical mechanism proposed by Kontani[20]. Very recently, an improved theoretical approach for the calculations of the critical temperature of conventional superconductors was proposed[21], but leads only to a moderate improvement in the calculated critical temperature for the specific case of YNi_2B_2C. The open questions about the superconductive phase and the nature of the superconducting gap anisotropy might relate to correlations in the electronic structure of YNi_2B_2C that have not been assessed so far.

Identifying electronic correlations in real materials is a delicate issue, that can be achieved by comparing the experimental spectroscopic data to ab-initio results. However, being many-body interactions by nature, electronic correlations pose a challenge for a proper theoretical treatment within density functional theory (DFT)[22]. Semilocal density functional approximations, such as the popular generalized gradient approximation (GGA), treat electrons as independent particles interacting via the mean field of the electron density. While vastly successful in predicting atomic structures, DFT-GGA is only able to describe a part of the correlation effects. This is particularly important in transition metals and lanthanides with partially filled d- and f-states, where the incomplete treatment of local (on-site) correlations in DFT-GGA often leads to discrepancies with experimentally observed energy bands. Local correlations are commonly applied by adding on-site Coulomb interaction U, either in a static (DFT+U), or frequency-dependent manner using dynamical mean field theory (DFT+DMFT)[23].

Here we present an experimental and theoretical study of the electronic structure of YNi_2B_2C beyond semilocal DFT. By comparing soft x-ray angle-resolved photoemission spectroscopy (SX-ARPES) data with state-of-the-art one-step photoemission calculations using DFT+DMFT, we identify the presence of moderate electronic correlations in this compound and provide an estimate in terms of values for the Coulomb U and exchange interaction J. We conclude that the influence of these electronic correlations on states close to E_F should be revisited by high-resolution ARPES and that their impact on superconductivity should also be considered in theoretical modelling.

Methods

Experimental methods

Soft x-ray ARPES experiments were performed at the SX-ARPES endstation[24] of the ADRESS beamline[25] of the Swiss Light Source using photons in the energy range $h\nu = 680$ eV to 900 eV. Using photons in the soft

[1]New Technologies-Research Centre, University of West Bohemia, 30100 Plzeň, Czech Republic. [2]Département de Physique and Fribourg Center for Nanomaterials, Université de Fribourg, CH-1700 Fribourg, Switzerland. [3]Institut Jean Lamour, UMR 7198, CNRS-Université de Lorraine, Campus ARTEM, 2 allée André Guinier, BP 50840, 54011 Nancy, France. [4]Paul Scherrer Institut, Swiss Light Source, 5232 Villigen PSI, Switzerland. [5]Institute for Quantum Materials and Technologies, Karlsruhe Institute of Technology, Kaiserstr. 12, D-76131 Karlsruhe, Germany. ✉e-mail: jminar@ntc.zcu.cz; claude.monney@unifr.ch

x-ray energy range increases the photoelectron escape depth by a factor of 3-5 compared to the ultraviolet energy range. This leads to increased bulk sensitivity and improved resolution in the k_z direction[26]. The experiments were performed for the (001) cleaved crystal surface at a temperature of 20 K to reduce thermal motion that would negatively affect the momentum selectivity[27]. Later, we refer to the momenta in the relative length units (r.l.u.), defined as 1 r.l.u. = $2\pi/a$, $2\pi/b$ and $2\pi/c$ in the k_x, k_y and k_z directions, respectively.

To reveal details of the SX-ARPES spectra, the broad, inelastic background in the experimental spectra is subtracted. Details of the background subtraction procedure are given in the Supplementary Note 2.

Theoretical methods

The full potential Korringa-Kohn-Rostoker (FP-KKR) calculations were performed with the spin-polarized relativistic Korringa-Kohn-Rostoker (SPRKKR) package[28] within the generalized gradient approximation (GGA) using the Perdew-Burke-Ernzerhof (PBE) exchange-correlation functional and basis set truncated at $l_{max} = 4$. In the SPRKKR package, the relativistic phenomena are included at the level of the Dirac equation.

The relativistic DFT+DMFT calculations were performed self-consistently with respect to the charge density and self-energy within the SPRKKR code, using the second order perturbative fluctuation exchange approximation (FLEX) solver[29,30]. The DFT+DMFT implementation follows the rotationally invariant LSDA+U formulation of Liechtenstein et al.[31]. The Slater integral F^0 is set equal to U, and the F^2 and F^4 are connected to J by the relations $J = (F^2 + F^4)/14$ and $F^4/F^2 = 0.625$. The DMFT parameters applied to Ni d-states ($U = 3.0$ eV, $J = 0.9$ eV and $T = 400$ K) are the same as determined for bulk Ni[29].

The one-step model of photoemission[32] used for ARPES simulations is implemented in the SPRKKR code[33]. The one-step model is based on Green's function and multiple scattering formalism and accounts for matrix element effects such as photon energy and polarization, experimental geometry, final state and surface effects. Therefore, the one-step model calculations allow direct comparisons to experimental ARPES spectra.

The matrix elements were calculated with the full potential formalism inside the muffin-tin spheres. The experimental geometry of the ADRESS beamline SX-ARPES endstation[24], with incoming photon direction 70° with respect to surface normal, was used in the ARPES simulations. Lifetime effects of the initial and final states were simulated by a constant imaginary part of the potential, 0.05 eV and 2.0 eV, respectively. To ensure that the momentum perpendicular to the surface, k_z, sampled in the one-step model calculations matches the experiment, we calculate a cut in the (k_x, k_z) plane by varying the photon energy. The results are presented in Supplementary Note 3.

In all calculations, the structural parameters were fixed to experimental values. The crystal structure is body-centered tetragonal (space group $I4/mmm$, no. 139, see Fig. 1a) with lattice parameters $a = 3.526$ Å and $c = 10.542$ Å. The structure consists of layers of yttrium (at Wyckoff position 2b) and carbon (at 2a), and layers of nickel (at 4d) surrounded by boron in distorted tetrahedral coordination (at 4e, $z_B = 0.1409$). The muffin-tin radii of the atom sites were set to 1.746 Å for Y, 1.243 Å for Ni, and 0.741 Å for B and C.

Results

Ground state electronic structure

In order to prepare the basis for studying the complex electronic band structure of YNi_2B_2C, we begin by looking at the bands calculated within DFT-GGA using the full potential KKR method (Fig. 1c). The relatively large unit cell with 4 atomic species produces a complex band structure with 18 bands contributing to the occupied states down to -11 eV. The most prominent feature are the Ni d-bands that almost exclusively form the states between the Fermi level and -4 eV. The majority of the band character between -6 eV and -11 eV comes from B and C (see also Supplementary Note 4).

However, as we will see below with SX-ARPES data, only a few bands appear with a significant photoemission spectral weight within 3 eV below the Fermi level. Therefore, to facilitate the comparison of the calculated band structure to the SX-ARPES spectra, we employ the one-step model of photoemission based on the multiple scattering KKR method. To this end, the prerequisite is a good quality set of scattering potentials calculated with the full potential KKR method, which we validate against the FP-LAPW method (see Supplementary Note 1). The excellent agreement between the band structures obtained with the FP-KKR, FP-LAPW and previously published band structures[18,34–36] ensures a reliable starting point for our one-step model simulations.

SX-ARPES and one-step model of photoemission

In Fig. 2b, f we show SX-ARPES data acquired with p-polarization at a temperature of 20 K. The photoemission intensity map along the path Z–Γ–Z at $k_z = 23$ r.l.u. ($h\nu = 693$ eV) in Fig. 2b has a bright A-shaped feature centered at Γ, extending from -0.5 eV down to -2.0 eV. In addition, less intense bands are observed dispersing up from -1.2 eV at Z, along with electron pockets at Γ and near Z. The one-step model spectrum calculated using the DFT-GGA in Fig. 2a captures well the main features and spectral

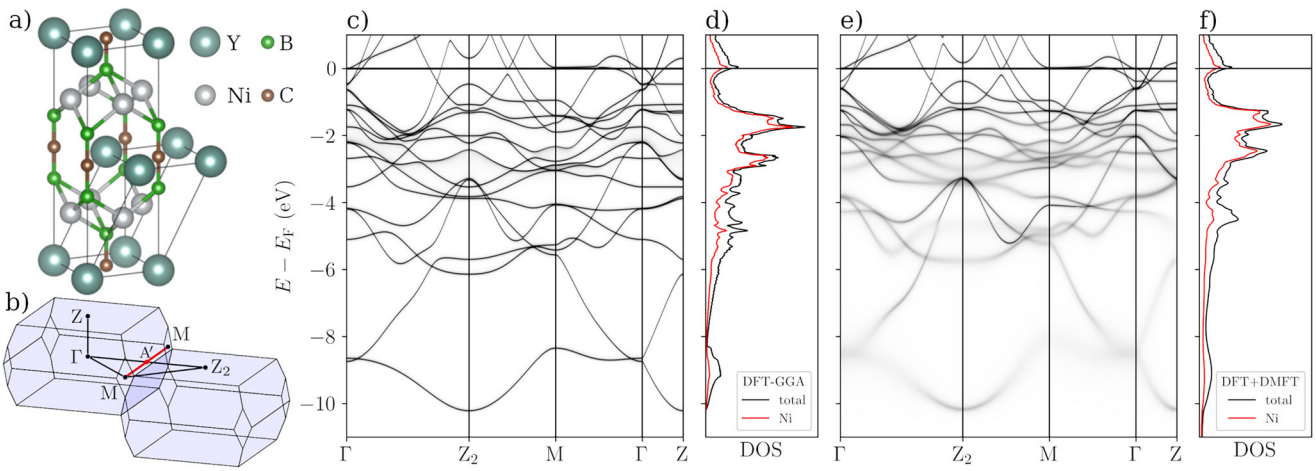

Fig. 1 | Crystal structure and electronic band structure of YNi_2B_2C. **a** Conventional and primitive unit cells of YNi_2B_2C. **b** Brillouin zone of YNi_2B_2C and the k-point path used in band structure calculations (black lines). The red line marks an additional path used in ARPES experiments and one-step model calculations. **c** Full potential KKR spectral function using the GGA. **d** DFT-GGA total DOS (black) and DOS projected on Ni d-states (red). **e** Full potential KKR spectral function within DFT+DMFT. **f** DFT+DMFT total DOS (black) and DOS projected on Ni d-states (red).

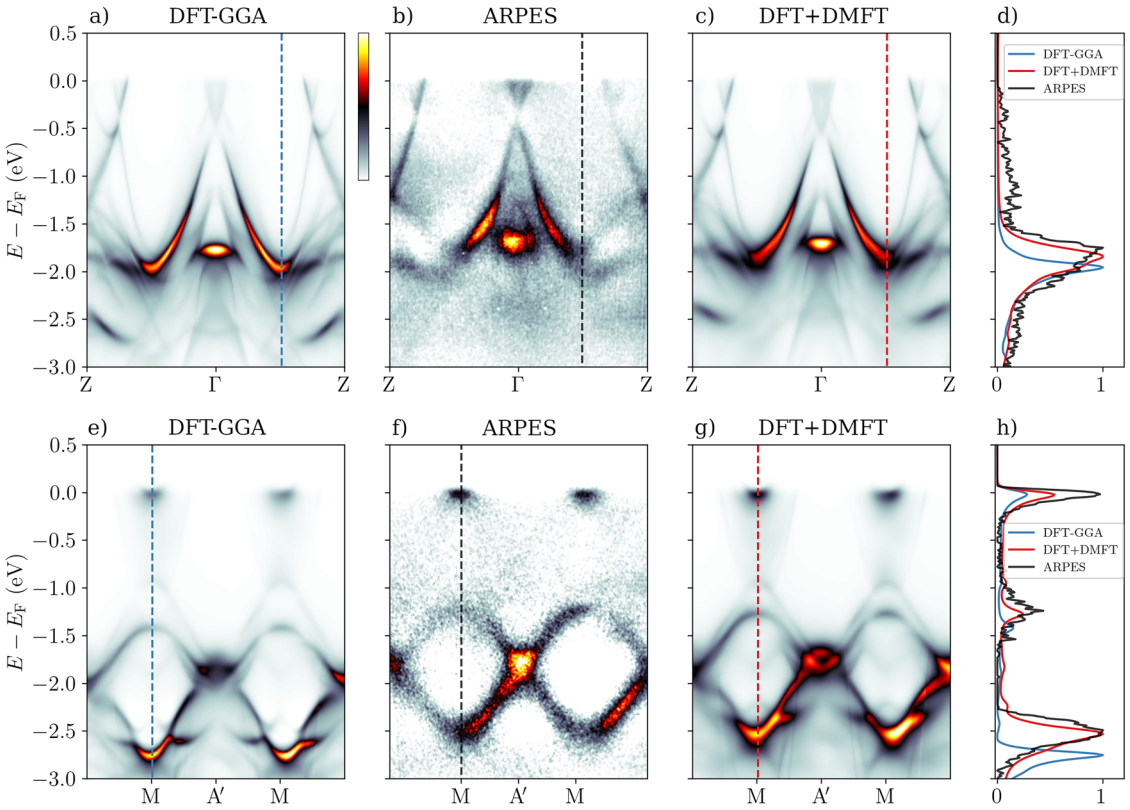

Fig. 2 | Comparison of experimental SX-ARPES (k,E)-maps to one-step model of photoemission. Comparison of one-step model spectra along the directions Z–Γ–Z (panels **a**–**c**) –and M–A′–M (panels **e**–**g**) at $k_z = 23$ r.l.u. calculated with DFT-GGA (panels **a** and **e**) and DFT+DMFT (panels **c** and **g**), and experiment using *p*-polarized light (panels **b** and **f**). Panels **d**, **h** show energy distribution curves (EDCs) taken at the positions indicated by dashed lines in panels **a**–**c** and **e**–**g**, respectively. The EDCs have been normalized so that the maximum value is 1.0.

weight distribution in the experimental spectrum in Fig. 2b. However, closer inspection reveals that the DFT-GGA bands near -2.0 eV are located higher in binding energy than in the experiment.

To access bands further away from E_F, we investigate a photoemission intensity map along the direction M–A′–M (see the BZ in Fig. 1b) at $k_z = 23$ r.l.u. (Fig. 2f). The ARPES data shows small electron pockets at the M points near E_F and ring-like features composed of upward and downward dispersing bands between -1.4 eV and -2.5 eV. The comparison to DFT-GGA one-step model result in Fig. 2e shows even larger shifts in band positions at higher binding energy, even though the overall shape of the intensity map is similar to experiment. The discrepancies are not explained by a rigid shift of the bands, because the electron pockets are correctly positioned close to E_F. Rather, it is a question of the well known delocalization problem caused by insufficient treatment of correlation effects in DFT-GGA[22], which leads to band width overestimation of partially filled *d*- and *f*-bands. We will therefore assess the effect of dynamical correlations to the ARPES spectra by comparing the one-step model spectra obtained with DFT+DMFT to the DFT-GGA and experimental spectra. A direct comparison between one-step model spectra and full potential KKR Bloch spectral function within DFT can be found in the Supplementary Note 5.

For this purpose we draw attention to the DOS in Fig. 1d. The majority of the states in the energy range -4 eV to E_F have Ni *d*-character. In addition, the Ni sublattice in YNi_2B_2C crystal structure (Fig. 1a) is strongly reminiscent of the structure of bulk Ni. Since the YNi_2B_2C lattice parameter *a* is very close to the lattice parameter of face centered cubic (fcc) Ni ($a_{Ni} = 3.524$ Å), the geometry of the square Ni planes YNi_2B_2C is essentially identical to the {001} planes of fcc-Ni. Therefore, to reduce the delocalization problem in the electronic structure, we choose to apply the DFT+DMFT to the *d*-states of Ni in YNi_2B_2C with the same parameters ($U = 3.0$ eV, $J = 0.9$ eV) as already determined for bulk fcc-Ni[29].

The DFT+DMFT band structure and DOS are presented in Fig. 1e, f. As DMFT is applied to the Ni *d*-states, the Ni bands between -1 eV and -4 eV shift towards the Fermi energy, reducing the *d*-band width. Most of the bands with mixed Ni and B character at energies from -4 eV to -10 eV do not shift significantly, but become very diffuse due to the imaginary part of the self-energy ImΣ. An exception is the band near the Z point with strongly mixed Ni and B character that shifts towards E_F by about 1.0 eV.

The one-step model spectra calculated with DFT+DMFT are presented in Fig. 2c, g. The electron pockets close to E_F at the M points in the M–A′–M spectra are not shifted, but the bands at higher binding energy are shifted towards E_F, leading to a very good agreement with the experimental spectra. To quantify the improvement brought by DFT+DMFT, we show energy distribution curves (EDCs) in Fig. 2d, h cut at in-plane momenta shown by dashed lines in Fig. 2a–c and e–g. Along the Z–Γ–Z direction (Fig. 2d), the DFT-GGA peak is 170 meV lower than the corresponding experimental peak, and DFT+DMFT shifts the peak up by 110 meV to a very good agreement with ARPES. In addition, the broadening of the bands by the imaginary part ImΣ of the self-energy leads to a wider peak shape in DFT+DMFT that corresponds more closely to the experiment. Along the M–A′–M direction (Fig. 2 h)), the bottom of the band at M is shifted up by 220 meV and the top of the band by 150 meV, bringing the peaks very close to the band positions in the experiment.

Finally, it is interesting to investigate if DFT+DMFT has an effect on the Fermi surface (FS) of YNi_2B_2C, as DFT band structure calculations have shown that the FS is well described already at the level of local density approximation (LDA)[19,36]. One-step model FS maps are compared to the SX-ARPES FS maps $k_z = 23$ r.l.u. ($h\nu = 693$ eV) and $k_z = 24$ r.l.u. ($h\nu = 760$ eV) in Fig. 3. Note that the contribution of the photon momentum $k_{phot} = h\nu/c$ has been subtracted so that the electron momentum $(k_x, k_y) = (0, 0)$ is at the center of the map. The experimental spectral weight distribution is very well reproduced by both DFT-GGA and DFT+DMFT,

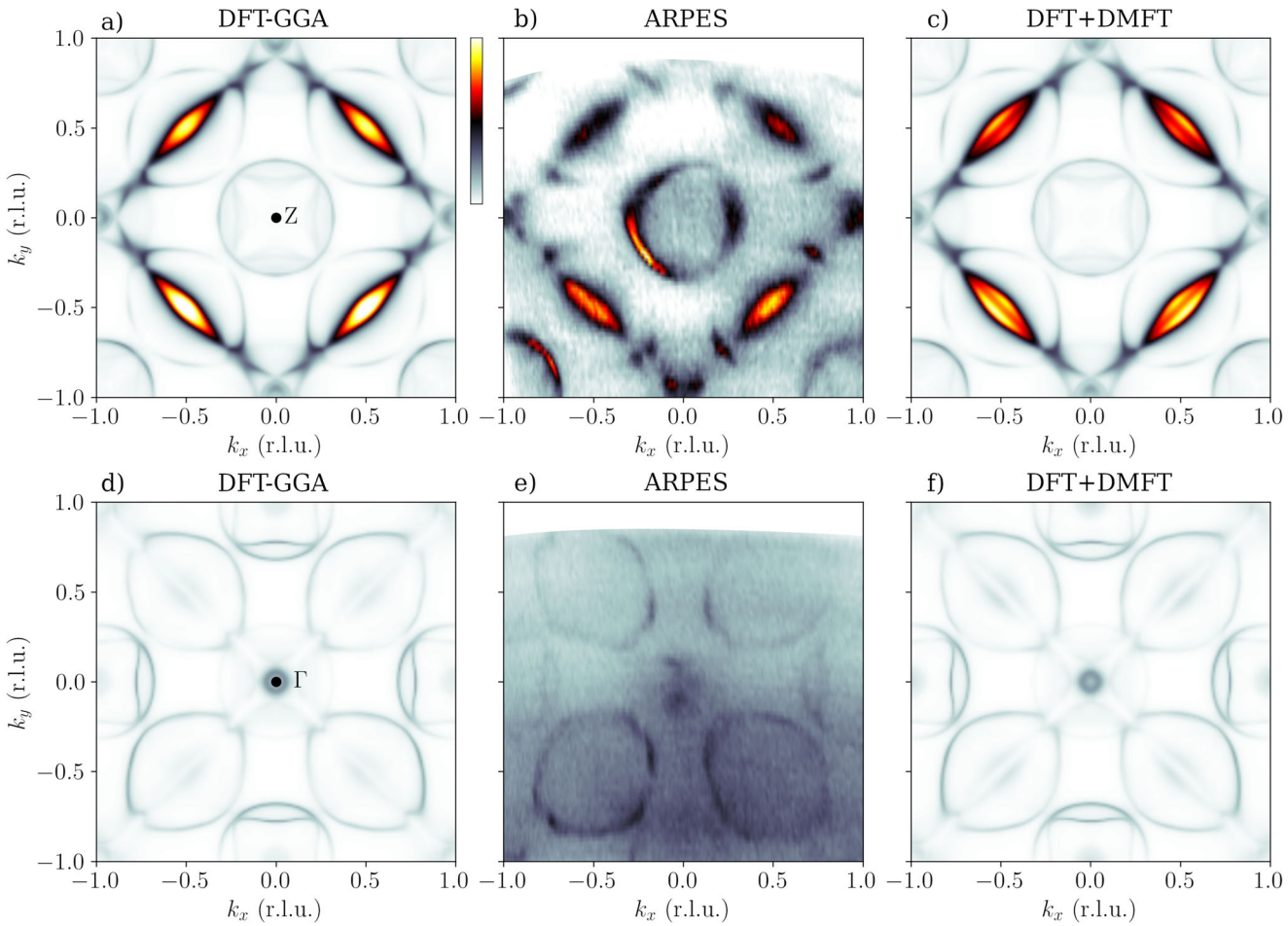

Fig. 3 | Comparison of experimental SX-ARPES Fermi surface maps to one-step model of photoemission. Comparison of Fermi surface maps at $k_z = 23$ r.l.u. (panels **a**–**c**) and $k_z = 24$ r.l.u. (panels **d**–**f**)), calculated with DFT-GGA (panels **a**, **d**) and DFT+DMFT (panels **c**, **f**), and experiment using *p*-polarized light (panels **b**, **e**). The high-symmetry point at the center of the map is indicated in panels **a**, **d**.

except for at the center of the map, where the experimental spectra has stronger spectral weight than either of the one-step model maps. The DFT-GGA and DFT+DMFT maps are remarkably similar, apart from a small increase of spectral weight at the Z points in the DFT+DMFT map in Fig. 3f), which we attribute to a downward shift of an Y-character band above E_F.

Our present work therefore evidences the presence of moderate, but substantial electronic correlations with $U = 3.0$ eV and $J = 0.9$ eV in the Ni *d*-states of YNi_2B_2C from an analysis of its electronic structure on a few-eV energy scale, indicating energy shifts of the order of 200 meV within 3 eV below the E_F. Now the question arises whether these electronic correlations affect substantially states close to E_F that are relevant for superconductivity and for anomalously broad phonon lineshape at low temperatures[19]. In the former case, Baba and coworkers identified with very high resolution ARPES the presence of superconductivity-induced band gaps in different Fermi surface pockets at a wave vector k_z value close to the Z point (which corresponds to $k_z = 23$ r.l.u. in our present notation)[17]. The band gaps were shown to be particularly large for the pockets close to $(k_x, k_y) = (0, 0)$. In the latter case, the electron-momentum dependence of electron-phonon coupling is substantially boosted by the presence of square-like pockets centered around $(k_x, k_y) = (0.5, 0.5)$ in the same k_z plane.

We have therefore calculated Fermi surfaces with DFT-GGA and DFT+DMFT ($U = 3.0$ eV, $J = 0.9$ eV), to assess the influence of electronic correlations beyond DFT-GGA (see Fig. 4) on these different contributions. A broadening of 1 mRy was used, meaning an integration over 14 meV around E_F.

Our calculations (Fig. 4a, b) show that, while moderate correlations do not affect the square-like pockets for $k_z = 0.5$ r.l.u. , they significantly modify the Fermi surface contributions near $(k_x, k_y) = (0, 0)$. As a comparison, we also show the FS calculated for $k_z = 0.0$ r.l.u. (Fig. 4c, d), for which similar trends are observed, but of smaller amplitude. These comparisons therefore support the idea that electronic correlations do not influence the electron-momentum dependence of electron–phonon coupling, as described by Kurzhals et al.[19] However, they suggest that the electronic states in the vicinity of the Fermi level that become gapped upon superconductivity are substantially modified by electronic correlations. Note that the ARPES measurements and one-step model calculations at integer k_z (23 r.l.u. and 24 r.l.u.) in Fig. 3 do not sample the square pockets which exist at half-integer k_z.

Our SX-ARPES data do not allow to resolve fine details in electronic dispersions on an energy scale of 10 meV to 30 meV that is relevant for superconductivity and renormalization of phonon lineshapes and we are unable to make a one-to-one comparison with experimental data. Additional low-energy ARPES data with sufficient high resolution, as in the study of Baba and coworkers, are therefore necessary to evaluate if our theoretical prediction is correct. In particular, it would be very helpful to map the electronic dispersions close to E_F for temperatures above and below the critical temperature of superconductivity.

What would be the consequence of moderate electronic correlations on Ni *d*-states? YNi_2B_2C has initially attracted attention as a potential Ni-based

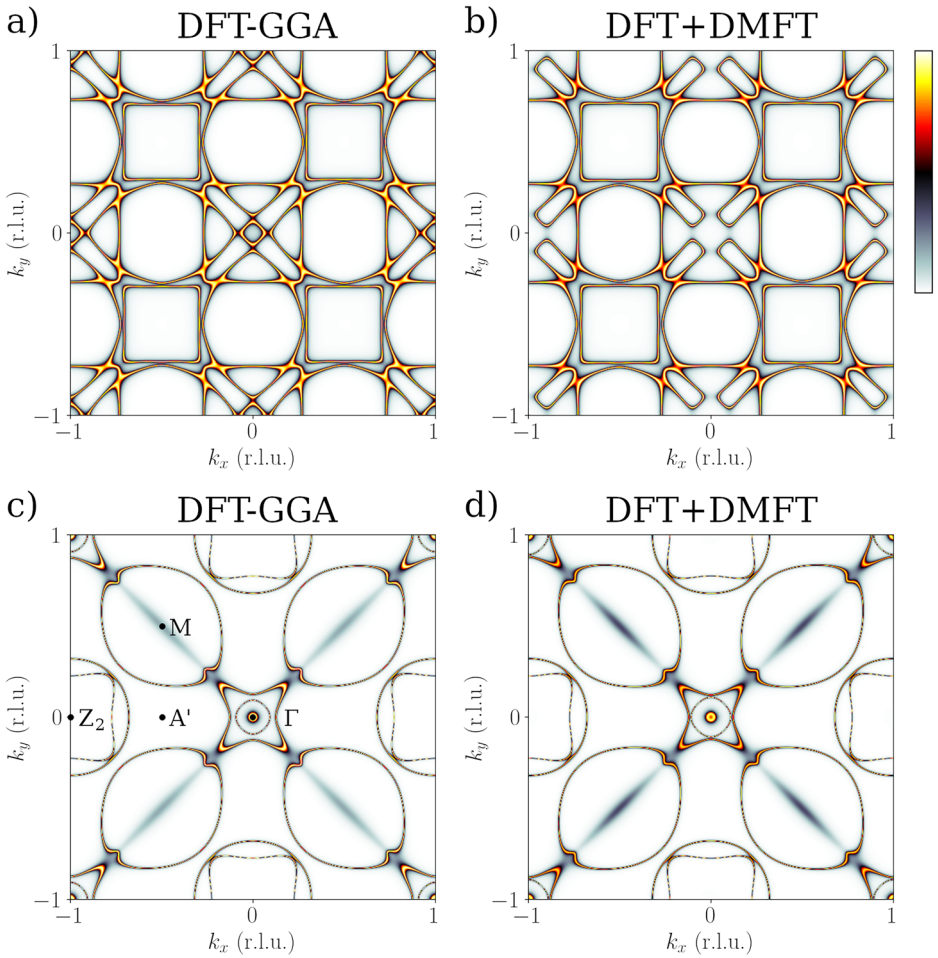

Fig. 4 | Bloch spectral function Fermi surface maps at $k_z = 0.5$ r.l.u. and $k_z = 0.0$ r.l.u. . Full potential KKR Bloch spectral function Fermi surface maps at $k_z = 0.5$ r.l.u. (**a**, **b**) and $k_z = 0.0$ r.l.u. (**c**, **d**), calculated with DFT-GGA (**a**, **c**), and DFT+DMFT ($U = 3.0$ eV, $J = 0.9$ eV). **b**, **d** Changes are observed near the center of the Brillouin zone, while the square-like pockets at $k_z = 0.5$ r.l.u. remain unaffected.

conventional superconductor with high critical temperature due to a phonon-mediated pairing interaction inducing a superconducting gap of about 2–3 meV[2–6,37]. However, a large anisotropy of the superconducting gap was later discovered, challenging the possibility of conventional superconductivity[7,10]. Recently, a theoretical approach based on the Eliashberg theory of superconductivity and including ab-initio static Coulomb interaction was used to calculate the critical temperature T_c of several conventional superconductors. It arrived this way to a value of T_c for the case of YNi_2B_2C about 25% lower than the experimental value. Interestingly, a very recent study reported an ab-initio calculation of the dynamically screened electron-electron Coulomb interaction leading to moderate electronic correlations with $U = 3$ eV. The same authors calculated a value of T_c even closer to the experimental one[38]. In that context, our work brings an experimental confirmation that moderate electronic correlations are present in YNi_2B_2C. This is particularly relevant in view of the work of Kontani[20]. In the proposed theory accounting for the anisotropic *s*-wave superconductivity, antiferromagnetic fluctuations originating from an on-site Coulomb interaction U were also treated within a FLEX-type approximation and play a central role. It would therefore be interesting to assess the necessary value for the magnetic interaction term in view of our estimation for U and J.

Conclusions

In this work, we compare one-step model calculations of photoemission using DMFT to SX-ARPES data and reveal the presence of moderate electronic correlations on the Ni *d*-states. In a recent work[19], it was demonstrated that electron-phonon coupling in YNi_2B_2C is strongly enhanced for specific values of electron momentum. Extrapolating from our SX-ARPES data and calculated Fermi surfaces, we anticipate that these moderate electronic correlations affect significantly the electronic states that participate in superconductivity and we propose very high resolution ARPES studies to assess this conjecture. These results, namely the moderate electronic correlations and momentum-dependent electron-phonon coupling, provide new fundamental input for models of superconductivity in YNi_2B_2C.

Data availability

The data supporting the findings of this article are openly available at https://doi.org/10.5281/zenodo.15260444.

Received: 29 September 2023; Accepted: 6 June 2025;
Published online: 17 June 2025

References

1. Cava, R. J. et al. Superconductivity in the quaternary intermetallic compounds $LnNi_2B_2C$. *Nature* **367**, (1994).
2. Mattheiss, L. F. Electronic properties of superconducting $LuNi_2B_2C$ and related boride carbide phases. *Phys. Rev. B* **49**, 13279–13282 (1994).
3. Mattheiss, L., Siegrist, T. & Cava, R. Superconductivity in the $LnNi_2B_2C$ intermetallics via boron A_{1g} phonons. *Solid State Commun.* **91**, 587–590 (1994).
4. Pickett, W. E. & Singh, D. J. $LuNi_2B_2C$: A novel Ni-based strong-coupling superconductor. *Phys. Rev. Lett.* **72**, 3702–3705 (1994).
5. Lee, J. I., Zhao, T. S., Kim, I. G., Min, B. I. & Youn, S. J. Electronic structure of Ni-based superconducting quaternary compounds: YNi_2B_2X (X=B, C, N, and O). *Phys. Rev. B* **50**, 4030–4033 (1994).

6. Lawrie, D. & Franck, J. Boron isotope effect in Ni and Pd based borocarbide superconductors. *Phys. C: Superconductivity* **245**, 159–163 (1995).
7. Nohara, M., Isshiki, M., Takagi, H. & Cava, R. J. Magnetic field dependence of the low-temperature specific heat of the borocarbide superconductor $LuNi_2B_2C$. *J. Phys. Soc. Jpn.* **66**, 1888–1891 (1997).
8. Nohara, M., Isshiki, M., Sakai, F. & Takagi, H. Quasiparticle density of states of clean and dirty s-wave superconductors in the vortex state. *J. Phys. Soc. Jpn.* **68**, 1078–1081 (1999).
9. Nohara, M., Suzuki, H., Mangkorntong, N. & Takagi, H. Impurity-induced gap renormalization in anisotropic superconductors: Mixed-state specific heat of $La_{2-x}Sr_x(Cu_{1-y}Zn_y)O_4$ and $Y(Ni_{1-x}Pt_x)_2B_2C$. *Phys. C: Superconductivity* **341–348**, 2177–2180 (2000).
10. Boaknin, E. et al. Highly anisotropic gap function in borocarbide superconductor $LuNi_2B_2C$. *Phys. Rev. Lett.* **87**, 237001 (2001).
11. Izawa, K. et al. Low energy quasiparticle excitation in the vortex state of borocarbide superconductor YNi_2B_2C. *Phys. Rev. Lett.* **86**, 1327–1330 (2001).
12. Izawa, K. et al. Gap function with point nodes in borocarbide superconductor YNi_2B_2C. *Phys. Rev. Lett.* **89**, 137006 (2002).
13. Maki, K., Thalmeier, P. & Won, H. Anisotropic s-wave superconductivity in borocarbides $LuNi_2B_2C$ and YNi_2B_2C. *Phys. Rev. B* **65**, 140502 (2002).
14. Martínez-Samper, P. et al. Phonon-mediated anisotropic superconductivity in the Y and Lu nickel borocarbides. *Phys. Rev. B* **67**, 014526 (2003).
15. Watanabe, T., Nohara, M., Hanaguri, T. & Takagi, H. Anisotropy of the superconducting gap of the borocarbide superconductor YNi_2B_2C with ultrasonic attenuation. *Phys. Rev. Lett.* **92**, 147002 (2004).
16. Weber, F. et al. Direct observation of the superconducting gap in phonon spectra. *Phys. Rev. Lett.* **101**, 237002 (2008).
17. Baba, T. et al. Angle-resolved photoemission observation of the superconducting-gap minimum and its relation to the nesting vector in the phonon-mediated superconductor YNi_2B_2C. *Phys. Rev. B* **81**, 180509 (2010).
18. Kawamura, M., Akashi, R. & Tsuneyuki, S. Anisotropic superconducting gaps in YNi_2B_2C: A first-principles investigation. *Phys. Rev. B* **95**, 054506 (2017).
19. Kurzhals, P. et al. Electron-momentum dependence of electron-phonon coupling underlies dramatic phonon renormalization in YNi_2B_2C. *Nat. Commun.* **13**, 228 (2022).
20. Kontani, H. Theory of anisotropic s-wave superconductivity with point-node-like gap minima: analysis of (Y, Lu)Ni2B2C. *Phys. Rev. B* **70**, 054507 (2004).
21. Pellegrini, C., Heid, R. & Sanna, A. Eliashberg theory with ab-initio coulomb interactions: a minimal numerical scheme applied to layered superconductors. *J. Phys.: Mater.* **5**, 024007 (2022).
22. Mori-Sánchez, P., Cohen, A. J. & Yang, W. Localization and delocalization errors in density functional theory and implications for band-gap prediction. *Phys. Rev. Lett.* **100**, 146401 (2008).
23. Georges, A., Kotliar, G., Krauth, W. & Rozenberg, M. J. Dynamical mean-field theory of strongly correlated fermion systems and the limit of infinite dimensions. *Rev. Mod. Phys.* **68**, 13–125 (1996).
24. Strocov, V. N. et al. Soft-X-ray ARPES facility at the ADRESS beamline of the SLS: concepts, technical realisation and scientific applications. *J. Synchrotron Radiat.* **21**, 32–44 (2014).
25. Strocov, V. N. et al. High-resolution soft X-ray beamline ADRESS at the Swiss Light Source for resonant inelastic X-ray scattering and angle-resolved photoelectron spectroscopies. *J. Synchrotron Radiat.* **17**, 631–643 (2010).
26. Strocov, V. N. et al. Three-dimensional electron realm in VSe_2 by soft-x-ray photoelectron spectroscopy: Origin of charge-density waves. *Phys. Rev. Lett.* **109**, 086401 (2012).
27. Braun, J. et al. Exploring the XPS limit in soft and hard x-ray angle-resolved photoemission using a temperature-dependent one-step theory. *Phys. Rev. B* **88**, 205409 (2013).
28. Ebert, H. et al. (2021). The Munich SPR-KKR package.
29. Minár, J. et al. Multiple-scattering formalism for correlated systems: A KKR-DMFT approach. *Phys. Rev. B* **72**, 045125 (2005).
30. Minár, J. Correlation effects in transition metals and their alloys studied using the fully self-consistent KKR-based LSDA+DMFT scheme. *J. Phys.: Condens. Matter* **23**, 253201 (2011).
31. Liechtenstein, A. I., Anisimov, V. I. & Zaanen, J. Density-functional theory and strong interactions: Orbital ordering in Mott-Hubbard insulators. *Phys. Rev. B* **52**, R5467–R5470 (1995).
32. Pendry, J. Theory of photoemission. *Surf. Sci.* **57**, 679–705 (1976).
33. Braun, J., Minár, J. & Ebert, H. Correlation, temperature and disorder: Recent developments in the one-step description of angle-resolved photoemission. *Phys. Rep.* **740**, 1–34 (2018).
34. Youn, S. J., Min, B. I. & Freeman, A. J. Large anisotropy in the optical conductivity of YNi_2B_2C. *Phys. Rev. B* **66**, 052512 (2002).
35. Yamauchi, K., Katayama-Yoshida, H., Yanase, A. & Harima, H. Band structure calculations and fermi surfaces of YNi_2B_2C. *Phys. C.* **412–414**, 225–229 (2004).
36. Weber, F. et al. Phonons and electron-phonon coupling in YNi_2B_2C. *Phys. Rev. B* **89**, 104503 (2014).
37. Cheon, K., Fisher, I. & Canfield, P. Boron isotope effect in single-crystal YNi_2B_2C and $LuNi_2B_2C$ superconductors. *Phys. C: Superconduct.* **312**, 35–39 (1999).
38. Christiansson, V. & Werner, P. Quaternary borocarbides: a testbed for DFT for superconductors. *Phys. Rev. B* **109**, L180505 (2024).

Acknowledgements

We thank our collaborators Philipp Kurzhals, Thomas Jaouen, Christopher W. Nicholson, Peter Nagel, Maxime Rumo and Björn Salzmann for their support during the ARPES measurements. A.P. and C.M. acknowledge support from the Swiss National Science Foundation Grant No. P00P2_170597. J.M. and A.P. would like to thank the project Quantum materials for applications in sustainable technologies (QM4ST), funded as project No. CZ.02.01.01/00/22_008/0004572 by P JAK, call Excellent Research.

Author contributions

A.P., J.M., and C.M. designed the research. A.P. and J.M. did the calculations. A.P. did the data analysis with help from G.K. All authors participated in the interpretation and discussion of the results. A.P. and C.M. wrote the paper, with input from G.K., V.N.S., F.W., and J.M.

Competing interests

The authors declare no competing interests.

Additional information

Supplementary information The online version contains supplementary material available at https://doi.org/10.1038/s42005-025-02180-4.

Correspondence and requests for materials should be addressed to Ján. Minár or Claude Monney.

Peer review information *Communications Physics* thanks the anonymous reviewers for their contribution to the peer review of this work.